molecular pharmaceutics

pubs.acs.org/molecularpharmaceutics

Article

Superparamagnetic Iron Oxide−Erastin−Polyethylene Glycol Nanotherapeutic Platform: A Ferroptosis-Based Approach for the Integrated Diagnosis and Treatment of Nasopharyngeal Cancer

Haonan Tang,[§] Xiao Zhou,[§] Lijuan Liu,[§] Ziyu Wang, Chen Wang, Ningbin Luo, and Guanqiao Jin*

Cite This: *Mol. Pharmaceutics* 2024, 21, 2767−2780

Read Online

ACCESS | Metrics & More | Article Recommendations

ABSTRACT: Erastin can induce ferroptosis in tumor cells as an effective small molecule inhibitor. However, its application is hampered by a lack of water solubility. This study investigated the effects of superparamagnetic iron oxide (SPIO)−erastin−polyethylene glycol (PEG) nanoparticles prepared by loading SPIO−PEG nanoparticles with erastin on ferroptosis. SPIO−erastin−PEG nanoparticles exhibited square and spherical shapes with good dispersibility. The zeta potential and hydrodynamic size of SPIO−erastin−PEG were measured as (−37.68 ± 2.706) mV and (45.75 ± 18.88) nm, respectively. On T_2-weighted imaging, the nanosystem showed significant contrast enhancement compared to no-enhancement magnetic resonance imaging (MRI). SPIO−erastin−PEG induced ferroptosis by increasing reactive oxygen species and iron content and promoting the accumulation of lipid peroxides and the degradation of glutathione peroxidase 4. Pharmacokinetic experiments revealed a half-life of 1.25 ± 0.05 h for the SPIO−erastin−PEG solution in circulation. Moreover, significant antitumorigenic effects of SPIO−erastin−PEG have been demonstrated in 5−8F cells and mouse-bearing tumors. These results indicated that the synthesized SPIO−erastin−PEG nanoplatform could induce ferroptosis effects in vitro and in vivo while exhibiting favorable physical characteristics. This approach may provide a new strategy for theranostic nanoplatform for nasopharyngeal cancer.

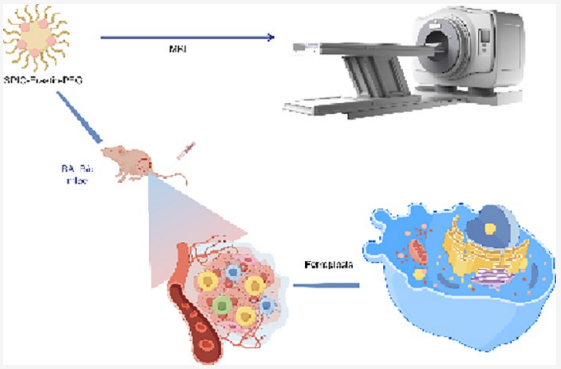

KEYWORDS: *ferroptosis, erastin, magnetic nanoparticles, pharmacokinetic, tumor therapy*

1. INTRODUCTION

According to 2021 data from the International Agency for Research on Cancer, over 100,000 new cases of nasopharyngeal carcinoma (NPC) were reported globally.[1] Moreover, the prevalence of the disease varies significantly across different regions of the world. More than 70% of new NPC diagnoses occur in East and Southeast Asia. It is common in the southern regions of China, with the highest incidence in Guangdong and Guangxi.[2] Over the past few decades, the treatment modalities for NPC have predominantly revolved around radiotherapy, chemotherapy, surgery, or their combinations.[3−5] Nonetheless, treatment failure in NPC is mainly due to tumor residue or recurrence at the primary site and distant metastasis.[6] Primary recurrence or distant metastasis caused by radiotherapy and chemotherapy resistance is still the core problem restricting the long-term survival of patients with NPC. To our knowledge, there is currently no accurate and noninvasive method for diagnosing and predicting the prognosis of NPC in real-time and guiding its clinical treatment.

In a considerable number of cancer types, iron-dependent lipid reactive oxygen species (ROS) accumulate during ferroptosis, leading to a new nonapoptotic form of cell death with tumor inhibitory effects,[7] and ferroptosis has been identified as a new target for cancer therapy. Its morphological, biochemical, and genetic characteristics differ from apoptosis, necroptosis, and autophagy.[8,9] Some literature on liver,[10] pancreatic,[11] prostate,[12] breast,[13] and other types of cancer[14] has demonstrated that ferroptosis can inhibit malignant cell proliferation. Notably, some highly malignant cancer cells are inherently vulnerable to ferroptosis, which has been developed as a potential novel method for cancer treatment. Erastin is a new compound discovered by Dolma et al. that can induce ferroptosis in a highly efficient, rapid, and sustained manner at very low concentrations.[15−17] It has been extensively studied as a ferroptosis inducer due to its potent ability to induce cell death in various tumors.[18] By inhibiting the activity of

Received: December 11, 2023
Revised: April 29, 2024
Accepted: April 30, 2024
Published: May 13, 2024

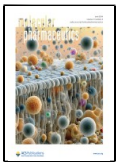

https://doi.org/10.1021/acs.molpharmaceut.3c01172
Mol. Pharmaceutics 2024, 21, 2767−2780

Scheme 1. Schematic Representation of the Preparation of SPIO−Erastin−PEG Nanoparticles

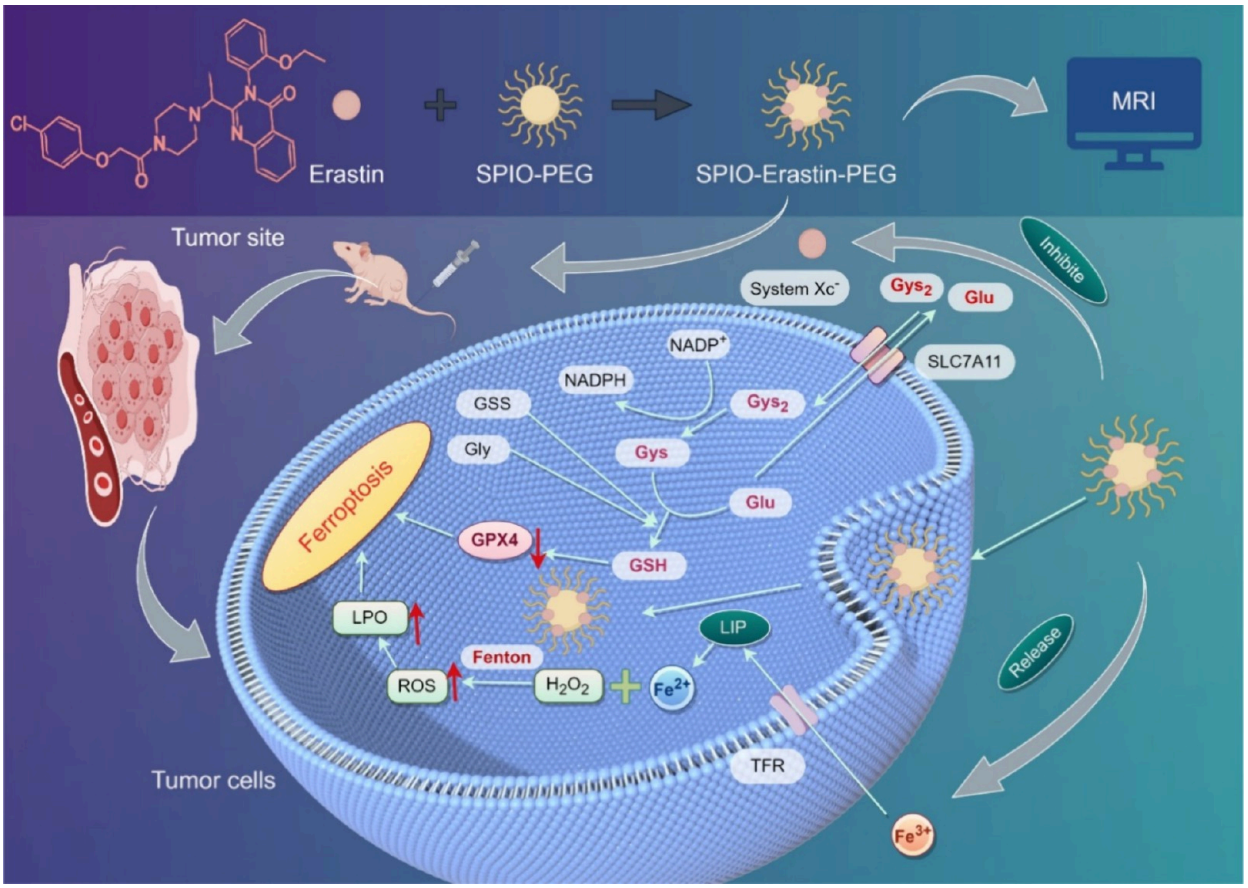

SLC7A11, the transporter subunit in System Xc−, erastin reduces the uptake of cystine, leading to a reduction in glutathione peroxidase 4 (GPX4) levels and ultimately inducing ferroptosis.[19] Previous studies have demonstrated that erastin inhibits the proliferation of NPC and enhances the responsiveness of NPC radiotherapy.[20,21] Ferroptosis induction erastin has great potential to become a new therapeutic approach that can overcome some of the limitations of conventional treatment methods. To avoid the disadvantage of the in vivo circulation process of erastin and to better exert targeted and efficient antitumor effects, erasin-based nanocarriers have become the research direction of drug delivery systems for integrated tumor diagnosis and treatment research.[22−24] Magnetic resonance imaging (MRI) of superparamagnetic iron oxide (SPIO) nanoparticles as a drug-delivery system for drug tracer function is a research hotspot in this field.[25,26] More importantly, SPIO can also increase the concentration of Fe^{2+} in cancer cells and promote the Fenton reaction to produce ROS, resulting in lipid peroxidation (LPO) in cells.[27] Our group has conducted extensive research on SPIO molecular imaging and the induction of ferroptosis in NPC.[28,29] Our study aims to synthesize an SPIO−erastin−PEG nano complex composed of polyethylene glycol (PEG)-coated SPIO nanoparticles coupled with erastin. In this drug-delivery system, erastin efficiently induces ferroptosis and plays a role in treating NPC. Simultaneously, it provides detailed tumor information through the magnetic resonance signal of SPIO. This not only provides an effective means for monitoring the treatment effect in real-time but also supplies timely and precise information for physicians to adjust treatment plans. The introduction of the ferroptosis mechanism and MRI technology in the SPIO−erastin−PEG system as an innovative therapeutic and diagnostic tool is mainly based on its unique role in the ferroptosis mechanism, which provides a novel and highly effective option for the integration of diagnosis and treatment of NPC (Scheme 1).

2. MATERIALS AND METHODS

2.1. Materials. The following materials were obtained: erastin (Aladdin Company, Shanghai, China), Fe_3O_4@OA (Dongna Biotechnology Co. Ltd., Nanjing, China), DSPE-mPEG solid powder (Tansh-Tech, Guangzhou, China), chloroform (Sinopharm Group Chemical Reagent Co. Ltd., Shanghai, China), four-channel animal coil (10F-04885, Teshen, Shenzhen, China), 3.0T MRI scanner (Discovery MR750, GE Healthcare, Chicago, USA), cell counting kit-8 (CCK-8) (Dojindo, Shanghai, China), rhodamine 6G (R6G) (Macklin, Shanghai, China), liproxstatin-1(Lip-1) (Selleck, Shanghai, China), deferoxamine mesylate (DFO) (Macklin, Shanghai, China), ROS assay kit (Beyotime, Shanghai, China), FerroOrange (Dojindo, Shanghai, China), TB Green Premix Ex *Taq*II (Tli RNaseH Plus) and PrimeScript RT Master Mix (Perfect Real Time) (TAKARA, Dalian, China), calcein/PI cell viability/cytotoxicity assay kit (Beyotime, Shanghai, China), mitochondrial membrane potential assay kit with JC-1 (Solarbio, Beijing, China), paraformaldehyde (Solarbio, Beijing, China), and hematoxylin and eosin(H&E) stain kit (Solarbio, Beijing, China). Human nasopharyngeal epithelial cell line NP69 was purchased from Guangzhou Cellcook Biotech Co., Ltd. Human NPC cell line SUNE-1 subline 5−8F

https://doi.org/10.1021/acs.molpharmaceut.3c01172
Mol. Pharmaceutics 2024, 21, 2767−2780

includes passage cells, and its primary cells were obtained from the American Type Culture Collection.

2.2. Synthesis of SPIO−Erastin−PEG. DSPE-mPEG was used as the primary raw material. Long-circulating micelles loaded with Fe_3O_4@OA and erastin were prepared by the reverse evaporation method. First, dissolved DSPE-mPEG (400 mg) and erastin (7 mg) were solubilized in chloroform (5 mL). The resulting solution was then transferred into an eggplant-shaped bottle, supplemented with Fe_3O_4@OA (20 mg) and purified water (10 mL), and ultrasonically shaken to form an emulsion. The probe was subjected to ultrasonic oscillation for 5 min at a power of 20%, with oscillation for 2 s and pausing for 3 s. Then, the flask was set onto a rotary evaporator and rotated at 70 °C in a water bath until no more bubbles were generated for 30 min. The solution was clear and translucent, with weak opalescence. The product was separated and purified using a 30k ultrafiltration tube. Finally, SPIO−erastin−PEG nanoparticles containing 1 mg mL^{-1} iron were synthesized.

2.3. Characterization of SPIO−Erastin−PEG and SPIO−PEG. Transmission electron microscopy (TEM) analysis was conducted using a JEM-2100 instrument (JEOL, Tokyo, Japan) to assess the size, shape, and dispersion characteristics of the SPIO−erastin−PEG nanoparticles. A Zetasizer Lab instrument (Malvern Panalytical, Malvern, USA) was utilized to assess the zeta potential and hydrodynamic size of SPIO−PEG and SPIO−erastin−PEG by dynamic light scattering (DLS). Additionally, the amount of erastin loaded onto SPIO−erastin−PEG was quantified using high-performance liquid chromatography (HPLC, Daojin).

2.4. In Vitro Stability and Hemolysis Assay of SPIO−Erastin−PEG. SPIO−erastin−PEG nanoparticles (100 μg mL^{-1}) were dispersed in equal volumes of phosphate-buffered saline (PBS), Roswell Park Memorial Institute (RPMI) 1640 medium, fetal bovine serum (FBS), Dulbecco's modified Eagle's medium (DMEM), and pure water (PW). The suspensions were left undisturbed for 7 days to observe any precipitation, thus evaluating the long-term size stability of SPIO−erastin−PEG nanoparticles in different media.

A hemolysis assay was conducted to assess the biocompatibility of the nanomaterial in the blood. In simple terms, varying concentrations of SPIO−erastin−PEG were thoroughly mixed with red blood cells (RBCs) and cultivated under standard conditions for 3 h at 37 °C in a 5% CO_2 incubator. Physiological saline and PW were used as positive controls (100% hemolysis) and negative controls (0% hemolysis), respectively. The absorbance of the supernatant was assessed at 540 nm using UV−visible spectrophotometry. The hemolytic rate was determined using the following formula:

$$Z\ (\text{hemolytic rate}) = (A - A_0)/(A_1 - A_0) \times 100\% \quad (1)$$

where A corresponds to the optical density (OD) of the sample group, A_1 is the OD of the positive control, and A_0 represents the OD of the negative control.

2.5. MRI of SPIO−Erastin−PEG, Erastin, and SPIO−PEG in Solution. Coronal T_2-weighted imaging (T_2WI) and T_2* mapping sequences were used for MRI imaging. Eppendorf tubes containing solutions of SPIO−PEG, SPIO−Erastin−PEG, and erastin at concentrations of 0, 0.01, 0.05, and 0.25 mg mL^{-1} were used to perform in vitro MRI experiments. Postprocessing MRI was utilized to generate T_2* mapping for various concentrations of SPIO−erastin−PEG, SPIO−PEG, and erastin.

2.6. Cellular Uptake. SPIO−erastin−PEG nanoparticle uptake by 5−8F NPC cells was investigated. The nanoparticles were modified with the fluorescent dye rhodamine 6G to enable fluorescence tracking. In a 24-well plate, 5−8F cells were added at a concentration of 1×10^5 mL^{-1} per well and incubated at 37 °C in a 5% CO_2 incubator for 24 h. The previous medium was then discarded, and rhodamine 6G-labeled R6G@SPIO−erastin−PEG nanoparticles (200 μg mL^{-1}) were added to the 24-well plate. The old medium was discarded and the cells were rinsed twice with PBS after 0, 1, 2, or 4 h of incubation at 37 °C in a 5% CO_2 incubator. Hoechst 33342 staining was applied for 30 min. Fluorescence microscopy was then used to observe the stained cells.

2.7. Detection of Intracellular Fe^{2+} Content. FerroOrange was employed to assess intracellular Fe^{2+} levels. Initially, 5−8F cells were plated at a concentration of 1×10^5 mL^{-1} per well in a 24-well plate and incubated for 24 h at 37 °C in a 5% CO_2 incubator, and the old medium was discarded. Then, the cells were rinsed twice with PBS to remove any residual substances. The control group consisted of 5−8F cells incubated with medium added.

In each well, SPIO−erastin−PEG (500 μL, 200 μg mL^{-1}) was added, and cell incubation was performed for 0, 2, 4, or 8 h at 37 °C in a 5% CO_2 incubator. Alternatively, separate wells received DFO (iron chelator), erastin, SPIO−PEG, SPIO−erastin−PEG, or SPIO−erastin−PEG + DFO, and cell incubation was performed for 4 h at 37 °C in a 5% CO_2 incubator. Following this, the FerroOrange probe (1 μmol L^{-1}) and fresh serum-free RPMI 1640 medium were introduced to each well, and cell incubation was further performed for 30 min at 37 °C in a 5% CO_2 incubator. Finally, fluorescence microscopy was used to capture fluorescence images.

2.8. Measurement of ROS Levels. First, inoculation of 5−8F cells into a 12-well plate with 1×10^5 mL^{-1} cells per well at 37 °C in 5% CO_2 was performed for 24 h. The old medium was discarded and washed twice with PBS to remove residual compounds, and 5−8F cells were treated with control, SPIO−PEG, erastin, and SPIO−erastin−PEG. The control group consisted of 5−8F cells incubated with medium. After 8 h, cells were stained with 2′,7′-dichlorofluorescin diacetate (DCFH-DA) (20 μM) (Beyotime, Shanghai, China) for 20 min in the dark at 37 °C, and the intracellular ROS levels were observed by fluorescence microscopy.

2.9. JC-1 Mitoscreen Assay. First, inoculation of 5−8F cells into a 12-well plate with 1×10^5 mL^{-1} cells per well at 37 °C in 5% CO_2 was performed for 24 h, followed by discarding the old medium and washing twice with PBS to remove residual substances. The control group consisted of 5−8F cells incubated with medium added. After treatment with control, SPIO−PEG, erastin, and SPIO−Erastin−PEG for 8 h, the mitochondrial membrane potential of 5−8F cells was detected using the JC-1 apoptosis detection kit (Solarbio, Beijing, China). This was performed following the kit instructions, and the cells were then visualized by fluorescence microscopy.

2.10. Colony Formation Assay. For the colony formation assay, inoculation of 5−8F cells into a 6-well plate with 1×10^4 mL^{-1} cells per well at 37 °C in 5% CO_2 was performed for 24 h. After discarding the old medium, the cells were thoroughly washed and rinsed with PBS to remove any residual substances. Subsequently, SPIO−PEG, erastin, and SPIO−

https://doi.org/10.1021/acs.molpharmaceut.3c01172
Mol. Pharmaceutics 2024, 21, 2767−2780

erastin−PEG were separately added to the wells, and the cells were cultured for 2−3 weeks. Following the incubation period, the cells were fixed for 30 min with 4% paraformaldehyde and visualized for 5 min with 0.1% crystal violet. Finally, ImageJ was used for analysis and quantification.

2.11. Wound Healing Assay. To perform the scratch assay, 5−8F cells were plated at a concentration of 1×10^7 mL^{-1} per well in a 6-well plate until they reached full confluency (100%). A gentle scratch was made in the center of each well using a 200 μL pipet tip. Then, SPIO−PEG, erastin, and SPIO−Erastin−PEG were applied to the cells. Images were captured at 0, 16, and 24 h under an inverted microscope. The scratch area was measured using ImageJ software to evaluate the migration capacity of the cells.

2.12. Western Blotting Analysis. Cells were lysed at 4 °C in RIPA lysis buffer containing PMSF (Solarbio, Beijing, China) at a 100:1 ratio. A bicinchoninic acid (BCA) protein assay kit (KeyGEN, Guangzhou, China) was used to determine the protein concentration. Equal amounts of protein (20 μg) were derived using sodium dodecyl sulfate-polyacrylamide gel electrophoresis (SDS-PAGE) on 10% gels. The proteins were then transferred to polyvinylidene difluoride membranes (Biosharp, Beijing, China). GPX4 (Abcam, ab125066, 1:1000) or β-actin (Abcam, ab8227, 1:1000) was then incubated on the membranes overnight at 4 °C after blocking with 5% nonfat milk in PBS. Membranes were incubated for 1 h with goat antirabbit IgG H&L (IRDye800CW) preadsorbed secondary antibody (Abcam, ab216773, 1:5000). An Odyssey DLx imaging system (Gene Company) was used to observe protein bands. The band density was measured by densitometry and quantified using ImageJ.

2.13. RNA Preparation and Real-Time Quantitative Polymerase Chain Reaction (RT-qPCR). Total RNA was extracted following the manufacturer's protocol using the total RNA kit (Beyotime, Shanghai, China). cDNA was synthesized using a PrimeScript RT master mix reagent kit. mRNA expression was examined by RT-qPCR using the TB Green Premix Ex *Taq*II reagent kit with primers and a qTOWER 3G real-time PCR detection system (Analytik Jena AG, Jena, Germany). Data were normalized to β-actin expression. The primer sequences (Sangon Biotech, Shanghai, China) were as follows:

β-actin-F: CCTGGCACCCAGCACAAT
β-actin-R: GGGCCGGACTCGTCATAC
GPX4-F: CCGCTGTGGAAGTGGATGAAGATC
GPX4-R: CTTGTCGATGAGGAACTGTGGAGAG

Amplification was performed under the following conditions: 95 °C for 30 s, followed by 40 cycles of 95 °C for 30 s and the specific annealing temperature for 30 s. The $2^{-\Delta\Delta CT}$ method with β-actin as an endogenous control was used to calculate relative gene expression. The results were presented as fold change values normalized to the controls.

2.14. GPX Activity Assessment. A cellular assay kit for detecting GPX levels, using nicotinamide adenine dinucleotide phosphate (NADPH) (Beyotime, Shanghai, China) as a cofactor, was utilized following the manufacturer's instructions. Shortly, cells were centrifuged at 12,000 × *g* for 10 min at 4 °C after mixing with lysis buffer on ice. For further assays, the resulting supernatant was collected. The control group included GPX detection buffer (50 μL) and GPX detection working fluid (40 μL), and the experimental group included the sample supernatant (20 μL), GPX detection buffer (20 μL), and GPX detection working fluid (50 μL). Samples were allowed to stand for 15 min at room temperature. Thereafter, 10 μL of a 30 mM peroxide reagent solution was added and mixed thoroughly. GPX activity was expressed as a ratio of the absorbance values of the control cells to the absorbance values of the mixture, measured at 340 nm, using a microplate reader.

2.15. Lipid Peroxidation Assessment. The level of lipid peroxidation was detected using the malondialdehyde (MDA) assay kit (Beyotime, Shanghai, China) following the manufacturer's protocol. Shortly, cells were centrifuged at 12,000 × *g* for 10 min at 4 °C after mixing with lysis buffer on ice. For further assays, the resulting supernatant was collected. After measuring the protein concentration, the supernatant sample (100 μL) was mixed with the test solution (200 μL) and incubated at 100 °C for 15 min. After cooling to 25 °C, the samples were centrifuged at 1000 × *g* for 10 min. The resulting liquid was collected as a supernatant. The MDA content is expressed as a ratio of the absorbance value of control cells to the mixture absorbance at 532 nm using a microtiter plate reader. The control group consisted of 5−8F cells incubated with medium.

Inoculation of 5−8F cells into a 12-well plate with 5×10^4 mL^{-1} cells per well at 37 °C in 5% CO_2 was performed for 24 h, followed by discarding the old medium and washing twice with PBS to remove residual substances. After treatment with control, SPIO−PEG, erastin, or SPIO−erastin−PEG for 8 h, each well received C11-BODIPY$^{581/591}$ to reach a final concentration of 10 μM, followed by a 30 min incubation period. Finally, inverted fluorescence microscopy was utilized for imaging.

2.16. Cytotoxicity of SPIO−erastin−PEG on NP69 and 5−8F Cells. NP69 and 5−8F cells, obtained during the exponential growth phase, were seeded at a density of 5×10^4 mL^{-1} in a 96-well plate. Then, plates were incubated for 24 h at 37 °C in 5% CO_2 in a constant temperature incubator with cell suspension (100 μL) added to each well. The medium was then replaced. There were six replicate wells in each of the experimental groups. SPIO−erastin−PEG, SPIO−PEG, erastin, and Lip-1 (1 μmol mL^{-1}) were supplied to 5−8F cells following the experimental requirements. Alternatively, SPIO−erastin−PEG was included in 5−8F and NP-69 cells. In addition, blank (fresh medium only) and control groups (fresh medium and 5−8F NPC cells only) were established. After 24 and 48 h of incubation at a constant temperature, the 96-well plate was taken out and rinsed three times with PBS. Fresh medium (90 μL) was then added to each well along with CCK-8 (10 μL) reagent. Microplates were incubated for 3 h at a constant temperature, and the absorbance at a wavelength of 450 nm was measured with a microplate reader (Molecular Devices, Shanghai, China). The following formula was used to calculate cell viability:

$$\text{cell viability}(\%) = [(\text{As} - \text{Ab})/(\text{Ac} - \text{Ab})] \times 100 \quad (2)$$

where Ab, Ac, and As represent absorbance in blank, control, and experimental wells, respectively.

2.17. Calcein/PI Viability Assay. To assess the viability of 5−8F cells, calcein/PI staining was performed. Initially, inoculation of 5−8F cells into 12-well plates with 1×10^5 mL^{-1} cells per well at 37 °C in 5% CO_2 was performed for 24 h. To eliminate any residual substances, cells were gently rinsed twice with PBS after removing the old medium. Subsequently, separate wells received SPIO−PEG, erastin, SPIO−erastin−PEG, and SPIO−erastin−PEG + DFO, followed by an additional 24 h incubation period. The cells

https://doi.org/10.1021/acs.molpharmaceut.3c01172
Mol. Pharmaceutics 2024, 21, 2767−2780

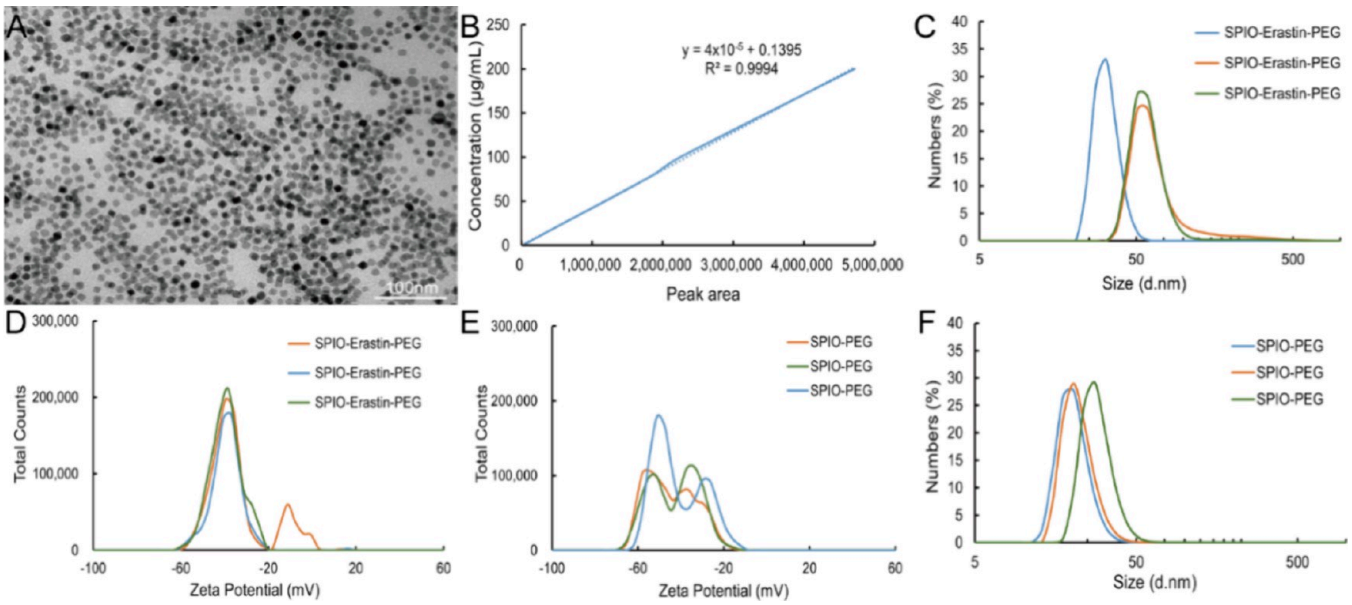

Figure 1. (A) TEM image of SPIO−erastin−PEG. (B) HPLC chromatogram of SPIO−erastin−PEG. (C, D) Hydrodynamic size and zeta potential of SPIO−erastin−PEG. (E, F) Zeta potential and hydrodynamic size of SPIO−PEG.

were then stained with calcein (1 μL) and PI (1 μL) solutions in the measurement buffer. After another 30 min incubation at 37 °C, an inverted fluorescence microscope was used to examine the cells. ImageJ software was used to measure the fluorescence intensities in each image.

2.18. Pharmacokinetic Study of SPIO−Erastin−PEG In Vivo. A group of 3 female C57 mice (6−8 weeks) was selected as the animal model. Initially, the mice were intravenously injected with SPIO−erastin−PEG (1 mg mL^{-1}, 200 μL) via the tail vein. At various time points (0, 5, 15, and 30 min, and 1, 2, 4, 8, and 24 h), blood samples (20 μL) were obtained by retro-orbital venous extraction. The blood samples were then treated with nitric acid and hydrogen peroxide for digestion and diluted to a specific volume. Finally, an inductively coupled plasma-optical emission spectrometer (ICP-OES) was used to determine Fe concentrations in various blood samples at different time points.

2.19. MRI of SPIO−Erastin−PEG In Vivo. The animal model for this study was carefully selected female BALB/c nude mice (4 weeks old). The animals strictly adhered to the approved protocol by Guangxi Medical University Cancer Hospital's Ethical Committee. 5−8F cells (100 μL, 1 × 10^7 mL^{-1}) were subcutaneously injected into the right hind limb. After injection of 0.2 mL SPIO−erastin−PEG (10 mg Fe^{-1} kg body weight) into 5−8F tumor-bearing BABL/c mice, in vivo monitoring experiments were conducted using a 3.0 T MRI scanner. The MRI sequences included axial T_2WI. BALB/c nude mice MRI images were acquired before and after injecting SPIO−erastin−PEG.

2.20. In Vivo Assessment of Antitumor Efficacy and Safety. The 5−8F tumor-bearing mice were randomly assigned to four groups (n = 5) when their tumors reached approximately 5 mm in diameter: control, erastin, SPIO−PEG, and SPIO−erastin−PEG. Intravenous injections were administered every other day, with a dosage of Fe (10 mg kg^{-1}) for each group and erastin (2.5 mg kg^{-1}). The control group received an equal volume of PBS. Throughout the treatment process, the nude mice were monitored daily for body weight and tumor size, starting on day 0 before to treatment. To determine tumor volume, length × width ^{2}/2 was multiplied by tumor size. If the tumor volume reached 2000 mm^3 or if the mice experienced a body weight reduction exceeding 15%, euthanasia was performed.

On day 16 after treatment, hearts, lungs, spleens, livers, kidneys, and tumors were harvested and fixed in 4% paraformaldehyde. Subsequently, the fixed tissues were subjected to H&E staining for microscopic study. K_i-67 and GPX4 staining were employed to evaluate tumor growth. A dihydroethidium (DHE) fluorescent probe was utilized to detect ROS levels in tumor tissues. Hematological analysis was carried out using an automated biochemical analyzer. Blood samples were collected from each mouse at 24 h after injection to measure biochemical and hematological parameters, thereby evaluating the safety of the nanoparticles.

2.21. Statistical Analysis. SPSS 23.0 and GraphPad Prism 8.0 were used for statistical analyses. Three replicates were performed for each experiment, and the data from each group were summarized as the mean ± standard deviation (x ± s). Independent samples t test and analysis of variance (ANOVA) were used to analyze differences. The LSD test was used to compare differences between groups. We considered a p-value of <0.05 statistically significant. Nonsignificant (ns) values were considered when $p > 0.05$, * $p < 0.05$, ** $p < 0.01$, *** $p < 0.001$, and **** $p < 0.0001$.

3. RESULTS AND DISCUSSION

3.1. Characterization of Nanoparticles. SPIO−erastin−PEG micelles loaded with Fe_3O_4@OA and erastin were prepared by the DSPE-PEG reverse evaporation method, and their characteristics were tested and verified. The TEM images revealed that most SPIO−erastin−PEG nanoparticles were square and spherical, and a few were polygonal. Furthermore, the dispersion of nanoparticles was favorable. The size of SPIO−erastin−PEG was 12.669 ± 1.341 nm and was relatively uniform (Figure 1A). The findings from the HPLC analysis indicated that the erastin loading rate of the SPIO−erastin−PEG nanoparticles was approximately 25% (Figure 1B). Compared with the hydrodynamic size (23.84 ± 4.418) nm

https://doi.org/10.1021/acs.molpharmaceut.3c01172
Mol. Pharmaceutics 2024, 21, 2767−2780

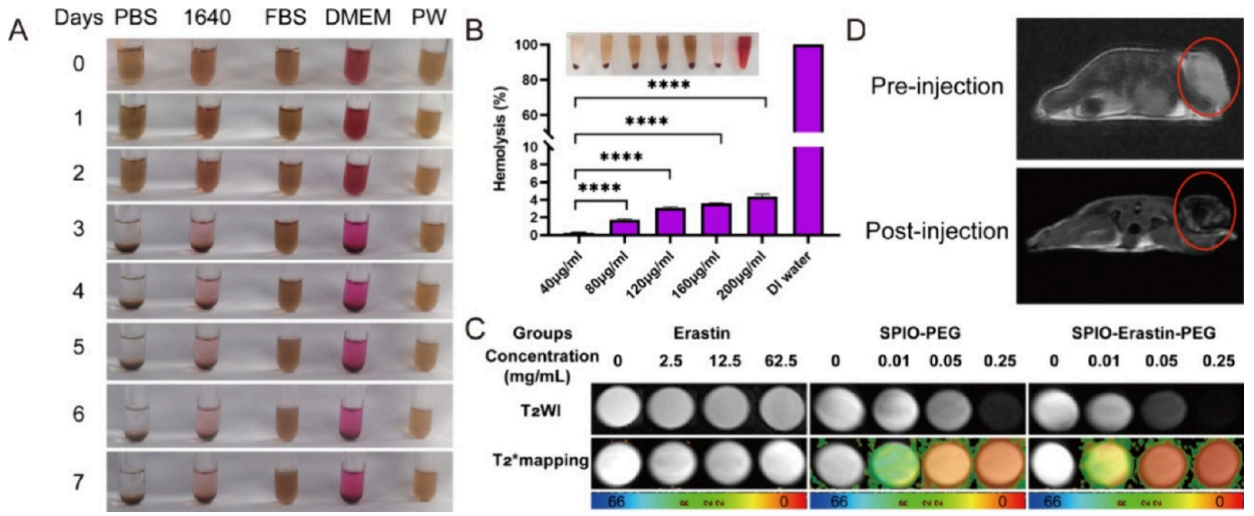

Figure 2. (A) In vitro stability of SPIO−erastin−PEG in different solutions. (B) Hemolysis test with different concentrations of SPIO−erastin−PEG. (C) T_2WI signal changes of SPIO−PEG, SPIO−erastin−PEG, and erastin in different concentrations. (D) T_2WI signal after injection of SPIO−erastin−PEG in 5−8F tumor-bearing nude mice.

and the zeta potential (−42.93 ± 1.652) mV of SPIO−PEG measured by DLS, SPIO−erastin−PEG showed a hydrodynamic size of 45.75 ± 18.88 nm and a zeta potential of −37.68 ± 2.706 mV (Figure 1C−F). The size of the target product DLS was slightly larger than that of SPIO−PEG, and the zeta potential was highly similar. This result indicated that erastin was successfully loaded onto SPIO−PEG. In addition, unlike other nanomaterials that require complex processing, the SPIO−erastin−PEG synthesized by our team did not require any specialized post-treatment. The nanoparticle platform simplified the operational protocol and eliminated the need for intricate steps or sophisticated equipment, thereby enhancing experimental efficiency and reproducibility.[30]

3.2. In Vitro Stability, Hemolysis Test, and MRI Monitoring Capability of SPIO−Erastin−PEG. SPIO−erastin−PEG nanoparticles were dispersed in various liquids, including PBS, RPMI-1640 medium, FBS, DMEM, and PW. The results revealed that no precipitation was observed in all measured liquids over 2 days. From day 3, PBS, RPMI 1640 medium, and DMEM had precipitation, while FBS and PW did not precipitate within 7 days. These results indicated that SPIO−erastin−PEG nanoparticles demonstrated excellent in vitro stability in FBS and PW (Figure 2A).

Blood compatibility is a crucial parameter for evaluating the biomedical application of materials within the body.[31] Therefore, a hemolysis test was conducted to assess the compatibility of nanoparticles with blood. In this test, the hemolytic activity of the released hemoglobin in the solution is directly proportional to the carrier's hemolytic activity. Consequently, the absorbance at 540 nm can be utilized to determine the hemolytic activity. As depicted in Figure 2B, no significant hemolysis was observed at different concentrations of nanoparticles. According to the absorbance value calculation results, all hemolysis rates were less than 5% when the nanoparticles were cocultured with RBCs. This indicated that SPIO−erastin−PEG had good blood compatibility and was suitable for further in vivo experiments.

In vitro MRI revealed that both SPIO−erastin−PEG and SPIO−PEG nanoparticles led to significant signal changes (T_2 relaxation time decreases) with increasing concentrations ($P < 0.05$). However, different concentrations of erastin showed no significant changes in signal intensity (Figure 2C) ($P > 0.05$). In vivo MRI results demonstrated a significant decrease in the T_2WI signal within the tumor region of the tumor-bearing nude mice following the injection of SPIO−erastin−PEG. This suggested that SPIO−erastin−PEG possessed molecular MRI capabilities, which could provide detailed tumor information through the MRI signal of SPIO (Figure 2D).

3.3. Cell Uptake and ROS Detection. Efficient uptake of nanoparticles by tumor cells is crucial for nanoparticles' ability to induce ferroptosis.[32] After successfully labeling SPIO−erastin−PEG with R6G, we monitored the cellular uptake of R6G@SPIO−erastin−PEG by 5−8F cells using fluorescence microscopy (Figure 3A,B). Upon analysis, we observed that when R6G@SPIO−erastin−PEG was cocultured with 5−8F cells, the red fluorescence of R6G mainly remained in the cytoplasm, indicating successful internalization of nanoparticles. Furthermore, red fluorescence could be observed in 5−8F cells as early as 1 h, and its fluorescence intensity increased over time, and the difference was statistically significant at different time points. These results demonstrated the efficient internalization and rapid localization of R6G@SPIO−erastin−PEG within 5−8F cells.

Moreover, when SPIO−erastin−PEG nanoparticles entered cells, Fe^{2+} levels significantly increased. To confirm this, we used FerroOrange, a cell-permeable fluorescent probe for intracellular ferrous ion detection, to monitor the levels of Fe^{2+} in 5−8F cells following various treatments. As shown in Figure 3C,D, the brightness of intracellular orange fluorescence increased with time after incubation of 5−8F cells with SPIO−erastin−PEG, suggesting that the intracellular concentration of nanoparticles accumulates continuously, consistent with the results of nanoparticle uptake by cells. To further confirm the influence of SPIO−erastin−PEG on intracellular ferrous ions, 5−8F cells were treated with DFO, erastin, SPIO−PEG, SPIO−erastin−PEG, and SPIO−erastin−PEG + DFO nanoparticles. As depicted in Figure 3E,F, cells treated with SPIO−erastin−PEG exhibited the strongest orange fluorescence, indicating the highest levels of Fe^{2+} production compared to others. The orange fluorescence in the control group and free DFO group was weak, and the fluorescence intensity of 5−8F cells treated by the SPIO−erastin−PEG +

https://doi.org/10.1021/acs.molpharmaceut.3c01172
Mol. Pharmaceutics 2024, 21, 2767−2780

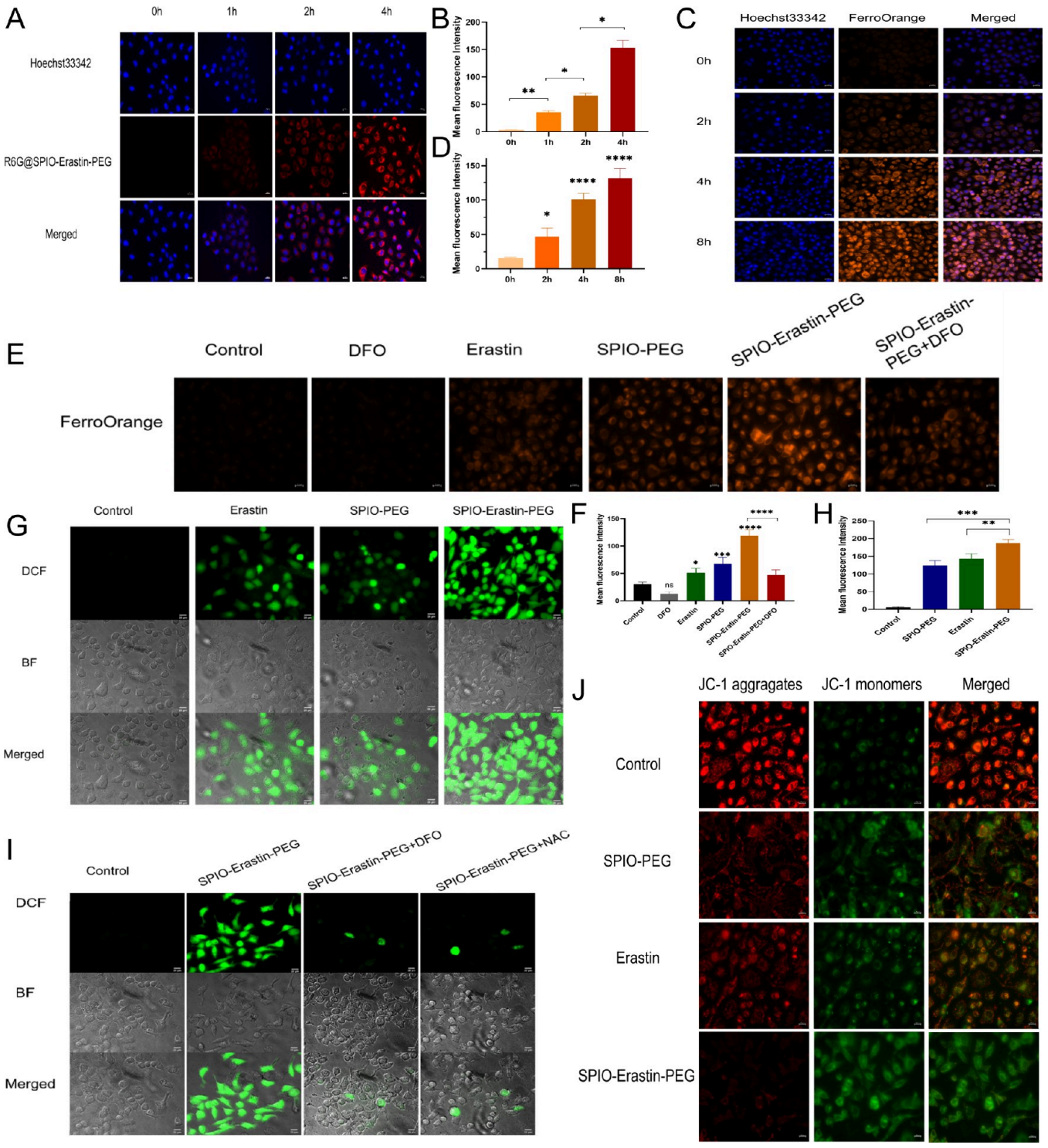

Figure 3. (A, B) R6G@SPIO−erastin−PEG nanoparticles in cells were observed and quantitatively analyzed by fluorescence microscopy at 0, 1, 2, and 4 h. (C, D) Fluorescence image and quantitative analysis of the change of intracellular Fe^{2+} content in SPIO−erastin−PEG nanoparticles during different culture times. (E, F) Fluorescence microscopy and quantitative analysis of intracellular Fe^{2+} content after treatment with DFO, erastin, SPIO−PEG, SPIO−erastin−PEG, and SPIO−erastin−PEG + DFO. (G−I) Evaluation of intracellular ROS levels in 5−8F cells after different treatments using the DCFH-DA method. (J) Impact of different treatments on the mitochondrial membrane potential of 5−8F cells.

DFO treatment group was significantly lower than that of SPIO−erastin−PEG treated cells, indicating that DFO significantly inhibited the production of Fe^{2+} in this group. Thus, SPIO−erastin−PEG nanoparticles were degraded to Fe^{2+} upon phagocytosis by 5−8F cells, thereby inducing cancer cell ferroptosis.

In addition, a large amount of Fe^{2+} production after being phagocytosed by 5−8 is further taken up by mitochondria and catalyzes the formation of ROS through the Fenton reaction.[33] This process increases the intracellular ROS concentration, leading to mitochondrial damage and ultimately cell death.[34] Erastin, an inducer of ferroptosis, can enhance the production

https://doi.org/10.1021/acs.molpharmaceut.3c01172
Mol. Pharmaceutics 2024, 21, 2767−2780

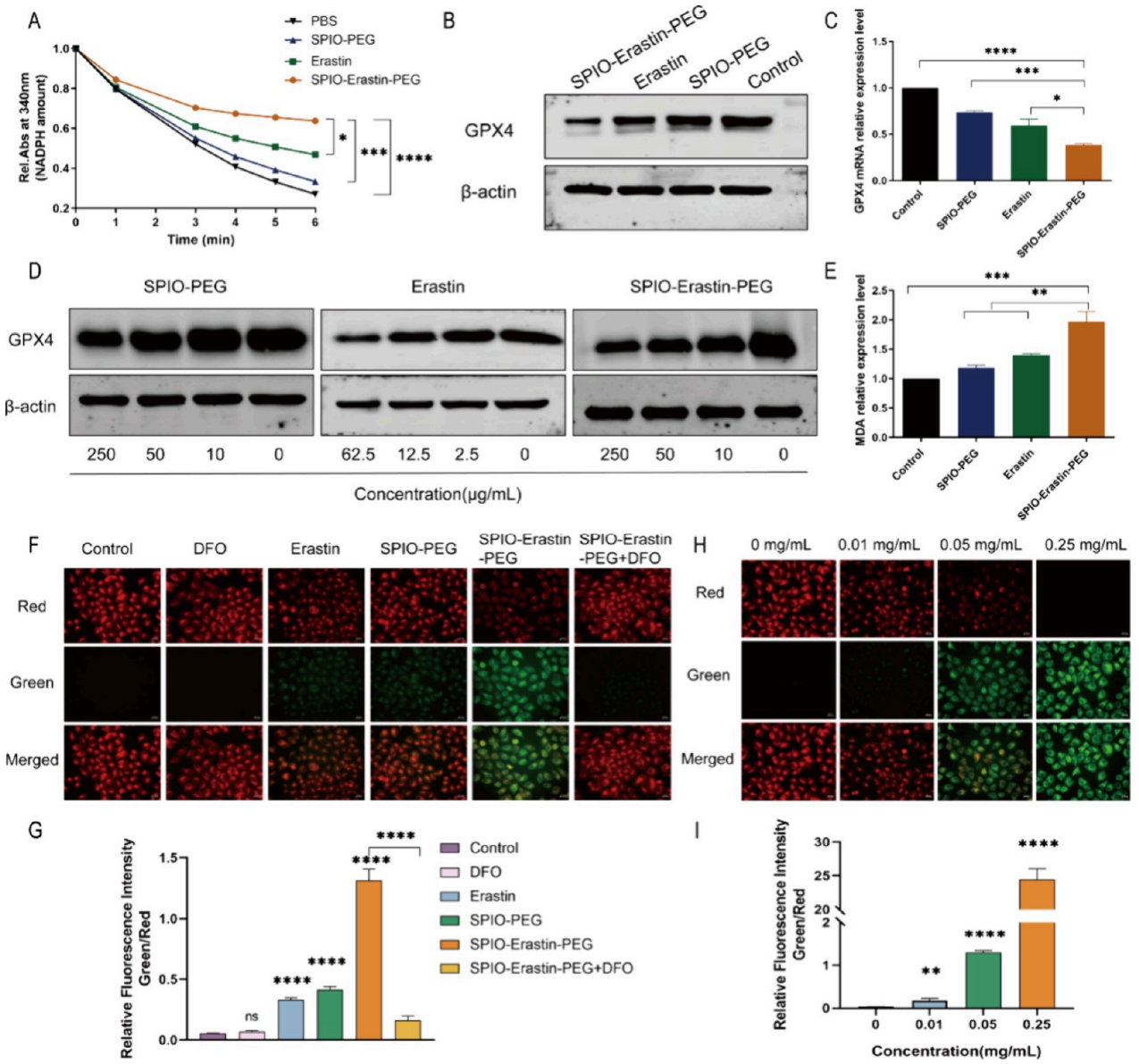

Figure 4. (A) Detection of GPX enzyme activity after treating 5−8F cells with free erastin, SPIO−PEG, and SPIO−erastin−PEG. (B, C) 5−8F NPC cells were divided into control, SPIO−PEG, erastin, and SPIO−erastin−PEG groups, and Western blotting and RT-qPCR were used to detect changes in GPX4 protein and mRNA expression levels. (D) The expression level of GPX4 was detected by Western blotting after treating 5−8F NPC cells with different concentrations of SPIO−PEG, erastin, and SPIO−erastin−PEG for 24 h. (E) Determination of the relative MDA content in tumor cells treated with free erastin, SPIO−PEG, and SPIO−erastin−PEG. (F−I) The levels of intracellular LPO in 5−8F cells following diverse treatments were illustrated and assessed through the C11-BODIPY $^{581/591}$ method.

of lipid ROS, thereby accelerating the occurrence of ferroptosis.[35] To investigate whether SPIO−erastin−PEG nanoparticles exacerbate intracellular ROS production, the probe DCFH-DA was utilized for detection. Figure 3G−I demonstrated that the intracellular green fluorescence intensity of the SPIO−erastin−PEG group significantly exceeded that of the erastin and SPIO−PEG groups. This finding indicated that the SPIO−erastin−PEG nanoparticles could generate substantial ROS. Pretreatment of the 5−8F cells in the SPIO−Erastin−PEG treatment group with the iron chelator DFO and the ROS inhibitor *N*-acetyl-L-cysteine (NAC) significantly reduced intracellular ROS levels. It was confirmed that SPIO−erastin−PEG nanoparticles induced ferroptosis by accelerating the generation of intracellular ROS production.

Mitochondria play a central role in cellular energy production, and it is essential to maintain normal cell proper function.[36] ROS-induced mitochondrial dysfunction is recognized as one of the early indicators of ferroptosis. To further examine the impact of SPIO−erastin−PEG nanoparticles on mitochondrial function, the JC-1 assay was used to detect changes in mitochondrial membrane potential in 5−8F cells. Typically, functional mitochondria exhibited red fluorescence in this assay, while depolarized mitochondria displayed green fluorescence. Additionally, the decrease of red fluorescence with the increase of green fluorescence signified mitochondrial dysfunction. The results showed that treatment with SPIO−erastin−PEG nanoparticles led to a rapid reduction in red fluorescence and a significant increase in green fluorescence within 5−8F cells compared to other treatment groups (Figure

https://doi.org/10.1021/acs.molpharmaceut.3c01172
Mol. Pharmaceutics 2024, 21, 2767−2780

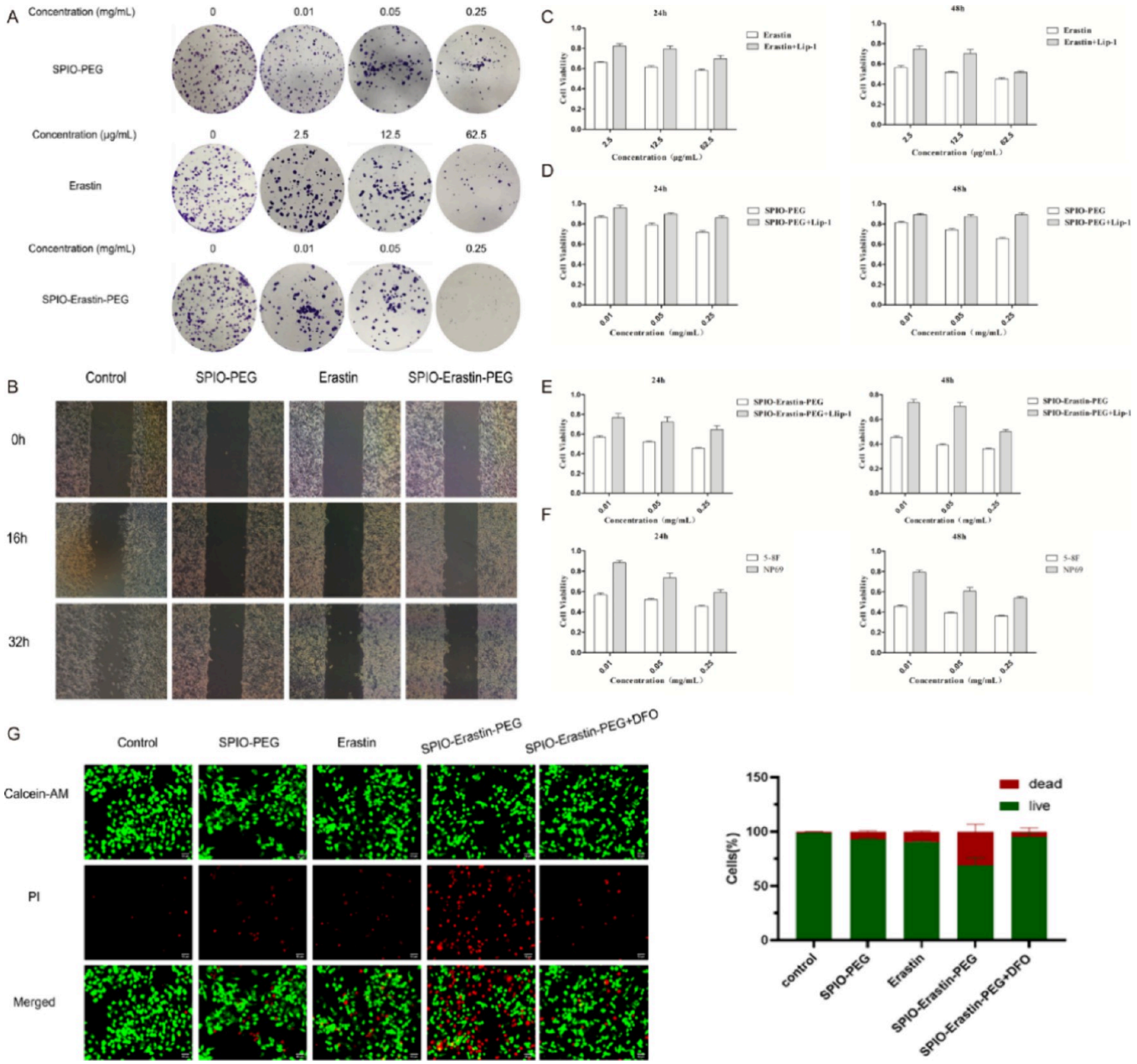

Figure 5. (A) Colony formation diagram of SPIO−PEG, erastin, and SPIO−erastin−PEG cocultured with 5−8F. (B) Cell migration diagram of 5−8F cells treated with free SPIO−PEG, erastin, and SPIO−erastin−PEG. (C) Viability of 5−8F cells cultured with erastin and Lip-1 for 24 and 48 h. (D) Viability of 5−8F cells following treatment with SPIO−PEG and Lip-1 for 24 and 48 h. (E) Viability of 5−8F cells following treatment with SPIO−erastin−PEG and Lip-1 for 24 and 48 h. (F) Viability of 5−8F cells or NP69 cells cocultured with SPIO−erastin−PEG nanoparticles for 24 and 48 h. (G) Fluorescence imaging of SPIO−erastin−PEG treated 5−8F cells with calcein/PI staining.

3J). The findings suggested that SPIO−erastin−PEG nanoparticles induced a decline in mitochondrial membrane potential in 5−8F cells, leading to mitochondrial dysfunction. Compared with other groups, SPIO−erastin−PEG was more beneficial in promoting tumor cell death through the multiple mechanisms mentioned above.

3.4. Molecular Mechanism of Ferroptosis Induced by SPIO−PEG, Erastin, and SPIO−Erastin−PEG in 5−8F Cells. During ferroptosis, the decreased activity of GPX (including GPX4) leads to excessive intracellular superoxide accumulation and lipid peroxidation, eventually leading to cell membrane damage and death. Therefore, the GPX detection kit based on the reduction of NADPH was used to evaluate GPX enzyme activity in each experimental group. Compared to the other treatment groups, the SPIO−erastin−PEG group had the slowest decrease in NADPH content within 3 min. Furthermore, regression analysis revealed that the GPX activity in the SPIO−erastin−PEG experimental group decreased by approximately 42% compared with the control group (Figure 4A).

To further clarify the molecular mechanism of ferroptosis induction, Western blotting and RT-qPCR were used to detect the changes in GPX4 expression levels in 5−8F cells treated with SPIO−PEG, erastin, and SPIO−erastin−PEG. The experimental results showed that GPX4 expression of SPIO−erastin−PEG treatment in 5−8F cells resulted in the most

https://doi.org/10.1021/acs.molpharmaceut.3c01172
Mol. Pharmaceutics 2024, 21, 2767−2780

significant decrease compared with the other treatment groups, indicating that this group was the most effective in inducing ferroptosis in NPC cells (Figure 4B,C) ($P < 0.05$). Moreover, GPX4 expression decreased with the gradual increase in the concentration of SPIO−PEG, erastin, and SPIO−erastin−PEG (Figure 4D; $P < 0.05$).

As the endproduct of lipid peroxidation, MDA is a crucial biomarker of cell ferroptosis.[37] Therefore, we further used the MDA assay kit to determine the content of lipid peroxidation in different experimental groups (Figure 4E). After 5−8F cells were treated with SPIO−erastin−PEG and incubated for 24 h, the oxidized lipid content in cells increased by 1.97 times. Meanwhile, the accumulation of lipid peroxidation in SPIO-Erstin-PEG-treated 5−8F cells was the most significant among all treatment groups, as observed by the C11-BODIPY$^{581/591}$ fluorescent probe. Furthermore, the green fluorescence intensity of the SPIO−erastin−PEG treatment group was significantly reduced after the addition of DFO, indicating that DFO could inhibit SPIO−erastin−PEG-induced intracellular lipid peroxidation (Figures 4F,G). In addition, we treated 5−8F cells with SPIO−erastin−PEG at different concentrations and observed the intracellular lipid peroxidation levels. As the concentration increased, the green fluorescence intensity in the cells increased, while the red fluorescence intensity decreased gradually. This indicates that lipid peroxidation level in 5−8F cells continuously increased (Figure 4H,I). These findings demonstrated that SPIO−erastin−PEG could induce ferroptosis in 5−8F cells.

3.5. In Vitro Antitumor Activity of SPIO−Erastin−PEG.

The plate colony formation assay was used to detect the effects of SPIO−PEG, erastin, and SPIO−erastin−PEG on cell proliferation. The results revealed a significant decrease in the growth rate and colony formation abilities of 5−8F cells treated with SPIO−Erastin−PEG compared to the control, erastin, and SPIO−PEG groups. Furthermore, these effects decreased in a dose-dependent manner with increasing drug concentrations. Statistical analysis revealed a significant difference in colony formation rate between each concentration and control group ($P < 0.05$). Notably, the SPIO−Erastin−PEG group displayed the lowest cell colony formation ability, indicating its pronounced inhibitory effect on 5−8F cell colony formation (Figure 5A; $P < 0.05$).

The effects of SPIO−PEG, erastin, and SPIO−erastin−PEG on the migration ability of 5−8F cells were detected by the wound healing assay. In the control group, the cell migration was slightly inhibited, and the cells gradually filled the scratch area with time. After 32 h, the scratched area became indistinguishable. In contrast, the SPIO−PEG, erastin, and SPIO−erastin−PEG groups exhibited varying degrees of cell migration inhibition (Figure 5B). Analysis of the scratch assay data at 32 h revealed the wound healing rates of the SPIO−PEG, erastin, SPIO−erastin−PEG, and control groups were 22.9% ± 2.1%, 16.2% ± 1.8%, 10.3% ± 2.5%, and 48.7% ± 4.0%, respectively ($P < 0.05$). These results clearly demonstrated that the SPIO−erastin−PEG group displayed the strongest ability to inhibit cell migration, providing valuable support for applying SPIO−erastin−PEG in tumor treatment.

The cell toxicity effects of erastin, SPIO−PEG, and SPIO−erastin−PEG were assessed using the CCK-8 cytotoxicity assay. The viability of 5−8F cells was observed to correlate with both the concentration and incubation time of erastin, SPIO−PEG, and SPIO−erastin−PEG (Tables 1−3; $P < 0.05$).

Table 1. Coculturing with Varying Concentrations of SPIO−Erastin−PEG Nanoparticles and the Viability of 5-8F Cells Was Assessed at Different Time Points

		cell viability	
concentration	n	24 h	48 h
0.01 mg mL^{-1}	6	56.89% ± 3.58%	52.11% ± 2.40%
0.05 mg mL^{-1}	6	45.42% ± 3.24%	39.26% ± 1.84%
0.25 mg mL^{-1}	6	39.15% ± 3.86%	33.90% ± 1.48%

Table 2. Coculturing with Varying Concentrations of SPIO−PEG Nanoparticles, the Viability of 5-8F Cells Was Assessed at Different Time Points

		cell viability	
concentration	n	24 h	48 h
0.01 mg mL^{-1}	6	86.44% ± 4.32%	79.07% ± 4.16%
0.05 mg mL^{-1}	6	81.41% ± 2.94%	74.27% ± 3.49%
0.25 mg mL^{-1}	6	71.86% ± 1.68%	63.70% ± 2.74%

Table 3. Coculturing with Varying Concentrations of Erastin Nanoparticles, the Viability of 5-8F Cells Was Assessed at Different Time Points

		cell viability	
concentration	n	24 h	48 h
2.5 μg mL^{-1}	6	66.31% ± 1.99%	56.56% ± 3.90%
12.5 μg mL^{-1}	6	61.53% ± 2.53%	51.76% ± 2.25%
62.5 μg mL^{-1}	6	58.20% ± 2.95%	45.21% ± 2.98%

Among these, SPIO−erastin−PEG induced cell death of 5−8F cells and was the most significant ($P < 0.05$). Moreover, the addition of Lip-1 partially restored cell viability (Figure 5C−E; $P < 0.05$). These findings suggested that erastin, SPIO−PEG, and SPIO−erastin−PEG induced ferroptosis in 5−8F cells.

To gain deeper insights into the mechanism of nanodrug-induced cell death, 5−8F and NP69 cells were incubated with SPIO−erastin−PEG. The results demonstrated that SPIO−erastin−PEG had a greater killing effect on tumor cells compared with NP69 cells (Figure 5F; $P < 0.05$). This difference could reflect higher levels of oxidative stress in tumor cells compared to normal cells, consistent with previous reports on ferroptosis.[38,39]

Furthermore, calcein/PI staining was employed to investigate the sensitivity of the 5−8F cells to SPIO−Erastin−PEG nanoparticles. The 5−8F cells were divided into control, SPIO−PEG, erastin, SPIO−Erastin−PEG, and DFO pretreated SPIO−Erastin−PEG groups. The treated 5−8F cells were incubated for 24 h before staining. As depicted in Figure 5G, the viable cells emitted green fluorescence, whereas the nonviable emitted red fluorescence. Almost all 5−8F cells in the control group showed bright green fluorescence, indicating minimal damage to the cancer cells. However, green and red fluorescence within 5−8F cells were observed in the SPIO−PEG, erastin, and SPIO−erastin−PEG groups, indicating a fraction of dead cancer cells. Notably, the SPIO−erastin−PEG group displayed the highest red fluorescence, signifying the strongest killing effect on 5−8F cells among all groups. This outcome was consistent with the CCK-8 cytotoxicity assay and provided cellular-level evidence for the highly effective antitumor performance of the SPIO−erastin−PEG nanoparticles. Additionally, pretreatment of the SPIO−erastin−PEG-treated group with ferroptosis inhibitor DFO significantly

https://doi.org/10.1021/acs.molpharmaceut.3c01172
Mol. Pharmaceutics 2024, 21, 2767−2780

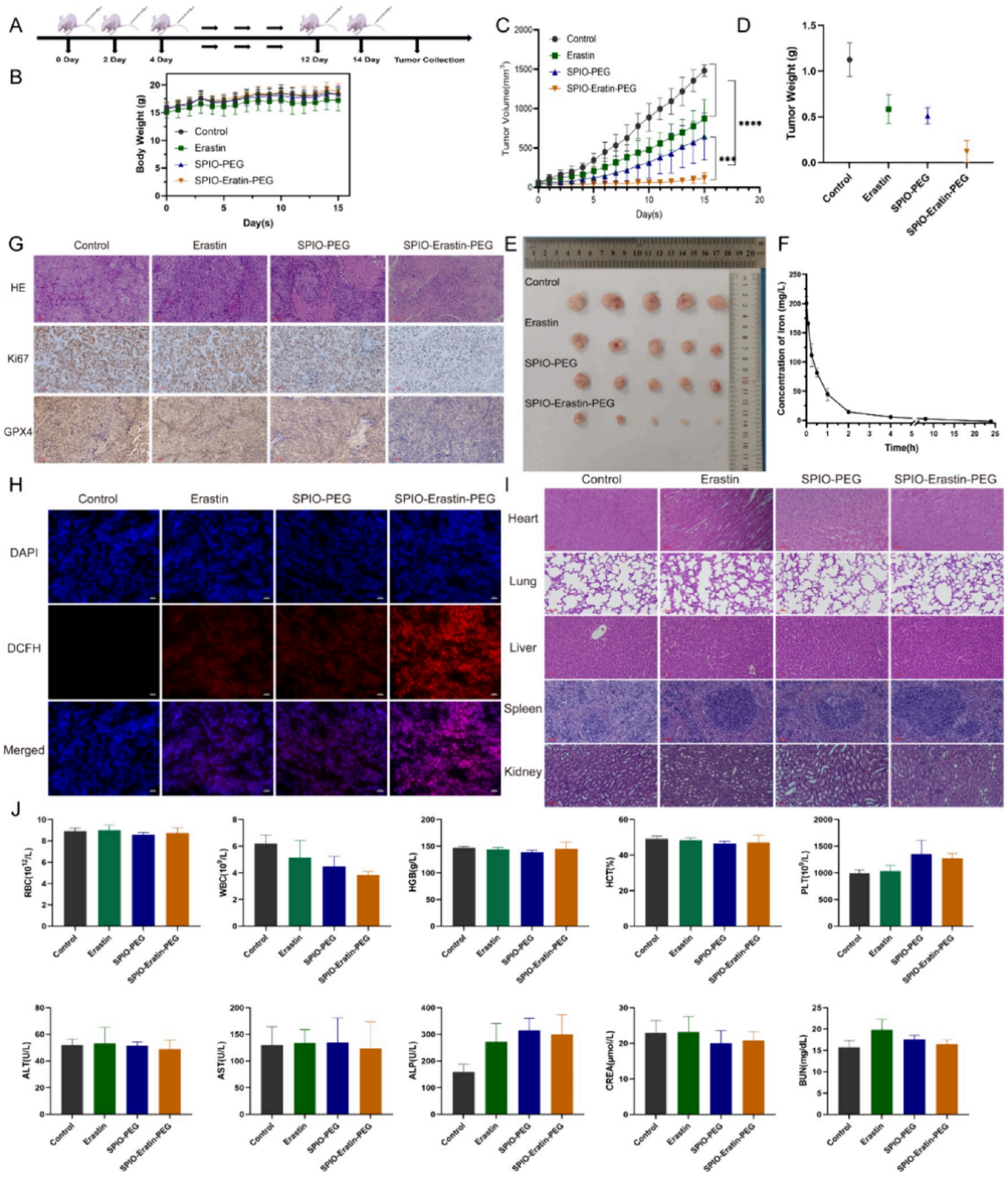

Figure 6. (A) Schematic representation illustrating the treatment process in 5−8F tumor-bearing nude mice. (B) Body weights of all 5−8F tumor-bearing nude mice during treatment. (C) Tumor volumes of all 5−8F tumor-bearing nude mice during treatment. (D) Tumor weights of all 5−8F tumor-bearing nude mice after different treatments. (E) Photographs of changes in tumor volume after different treatments. (F) Pharmacokinetic analysis of SPIO−Erastin−PEG. (G) H&E-stained, K_i-67 antigen, and GPX4 immunohistochemical staining images of tumors from different treatment groups, scale bar = 50 μm. (H) ROS levels in tumor tissues were assessed through immunofluorescence staining with DHE, scale bar = 20 μm. (I) H&E staining of the heart, liver, spleen, lung, and kidney after various treatments, scale bar = 50 μm. (J) Hematology analysis of treated mice. The terms include RBC, white blood cell, hemoglobin (HGB), hematocrit (HCT), platelet (PLT), alanine aminotransferase (ALT), aspartate aminotransferase (AST), alkaline phosphatase (ALP), creatinine (CREA), and blood urea nitrogen.

https://doi.org/10.1021/acs.molpharmaceut.3c01172
Mol. Pharmaceutics 2024, 21, 2767−2780

reduced cell death in 5−8F cells, suggesting the inhibition of the ferroptosis pathway induced by the SPIO−erastin−PEG nanoparticles.

3.6. In Vivo Antitumor Activity of SPIO−Erastin−PEG.

After observing the significant antitumor effect of SPIO−erastin−PEG on 5−8F cells in vitro, the ferroptosis effect of SPIO−erastin−PEG was further tested in 5−8F tumor-bearing nude mice. Twenty tumor-bearing nude mice (n = 5 per group) were randomly divided into four groups: control group (PBS), erastin group, SPIO−PEG group, and SPIO−erastin−PEG group. Once the tumor diameter reached about 5 mm, mice in each group commenced the 16 day treatment regimen, as depicted in Figure 6A. Specifically, tail vein injections were administered every other day. Furthermore, the body weight and tumor volume of 5−8F tumor-bearing nude mice were recorded daily throughout the treatment period.

Based on the data in Figure 6B, the body weight of 5−8F tumor-bearing nude mice remained relatively stable in each treatment group. It did not change significantly compared with PBS-treated controls. This suggested that all treatment groups had minimal toxic effects in nude mice. Moreover, the relationship between treatment time and measured tumor volume is depicted in Figure 6C−E. The results indicated that the tumor volume of the control group treated with PBS continued to increase throughout the treatment period. In contrast, the SPIO−erastin−PEG group exhibited significant tumor growth inhibition with an impressive suppression rate of 93%.

Due to the inadequate water solubility and metabolic instability of erastin in the body, its half-life in the bloodstream is less than 5 min, which is unsuitable for direct in vivo drug administration.[40] However, nanoparticles have demonstrated superior therapeutic effects compared to free drugs due to their high permeability and long retention time in solid tumors. Therefore, it is essential to design nanomedicine with properties that prolong blood circulation. In this study, SPIO−erastin−PEG nanoparticles were synthesized by combining erastin with SPIO−PEG to enhance their blood retention ability. To assess the behavior of these nanoparticles in the bloodstream, we performed a pharmacokinetic analysis of iron content in blood using ICP-OES. The results showed that after intravenous injection of SPIO−erastin−PEG, the Fe content in the blood decreased to 78% ID mL^{-1} after 1 h, while 22% of SPIO−erastin−PEG remained in circulation (Figure 6F). Furthermore, the blood circulation half-life of SPIO−erastin−PEG was increased to 1.25 ± 0.05 h (Table 4). Therefore, the pharmacokinetic results indicated that SPIO−Erastin−PEG nanoparticles effectively improved the solubility and stability of erastin in vivo and significantly prolonged its half-life in blood circulation.

Table 4. Pharmacokinetic Parameters of SPIO−Erastin−PEG after a Single Intravenous Dose to C57[a]

pharmacokinetic parameters	SPIO−erastin−PEG
half-life (h)	1.25 ± 0.05
CL (h L^{-1})	1.23 ± 0.16
MRTlast (h)	1.28 ± 0.06
AUClast (h*mg L^{-1})	159.51 ± 13.33

[a]Abbreviations: CL, clearance; MRT, mean residence time; AUC, area under the curve.

Histopathological analysis was conducted on the tumor samples to further evaluate the influence of various drugs on tumor tissue (Figure 6G). First, H&E staining was performed to reveal the microscopic damage to the nucleus and cytoplasm of the tumor cells in the SPIO−erastin−PEG treatment group. Immunohistochemical staining of the K_i-67 antigen demonstrated that its expression significantly decreased after treatment with SPIO−erastin−PEG nanoparticles, indicating that the tumor proliferation ability was weakened. Furthermore, the immunohistochemical analysis demonstrated that the expression level of GPX4 was significantly reduced in tumors of SPIO−erastin−PEG-treated nude mice compared to the other three groups, implying that SPIO−erastin−PEG induced ferroptosis. DHE staining analysis depicted in Figure 6H showcased that tumors of nude mice treated with SPIO−erastin−PEG had the highest level of ROS accumulation among all treatment groups, indicating an induced ferroptosis effect. Considering the physicochemical properties and in vivo antitumor efficacy, it can be inferred that SPIO−erastin−PEG had a pronounced ability to inhibit the growth of NPC.

To assess the biocompatibility of the synthesized nanoparticles, the hearts, livers, spleens, lungs, and kidneys of 5−8F tumor-bearing nude mice were subjected to various treatments and stained with H&E staining (Figure 6I). The findings revealed no notable pathological abnormalities in the major organs of mice in different treatment groups, indicating a healthy state. Moreover, hematological analysis was performed to evaluate the in vivo toxicity of SPIO−erastin−PEG nanoparticles. The results of routine blood and serum biochemical analyses were within normal ranges, indicating that SPIO−erastin−PEG nanoparticles did not induce significant systemic toxicity in vivo (Figure 6J). In summary, SPIO−erastin−PEG nanoparticles showed potent antitumor performance in vivo through ferroptosis induction and a good safety profile.

4. CONCLUSIONS

In conclusion, we have successfully fabricated the SPIO−erastin−PEG nanotherapeutic platform, which has several advantages. It shows stable performance in vivo and in vitro, can accurately deliver drug doses and has good MRI tracking ability. More importantly, it induces ferroptosis by changing the tumor microenvironment to exert antitumor efficacy. This breakthrough provides a fresh perspective for integrating the diagnosis and treatment of NPC, which may help overcome the limitations of conventional therapies and offer a new means for its diagnosis and treatment.

AUTHOR INFORMATION

Corresponding Author

Guanqiao Jin − *Guangxi Medical University Cancer Hospital, Nanning 530021, China*; Email: jinguanqiao77@gxmu.edu.cn

Authors

Haonan Tang − *Guangxi Medical University Cancer Hospital, Nanning 530021, China*; orcid.org/0000-0002-2917-6662

Xiao Zhou − *Xiangtan Central Hospital, Xiangtan, Hunan 411000, China*

Lijuan Liu − *Guangxi Medical University Cancer Hospital, Nanning 530021, China*; orcid.org/0000-0002-8326-0371

https://doi.org/10.1021/acs.molpharmaceut.3c01172
Mol. Pharmaceutics 2024, 21, 2767−2780

Ziyu Wang − *Guangxi Medical University Cancer Hospital, Nanning 530021, China*
Chen Wang − *Guangxi Medical University Cancer Hospital, Nanning 530021, China;* orcid.org/0000-0002-2725-601X
Ningbin Luo − *Guangxi Medical University Cancer Hospital, Nanning 530021, China*

Complete contact information is available at: https://pubs.acs.org/10.1021/acs.molpharmaceut.3c01172

Author Contributions

§H.T., X.Z., and L.L. contributed equally to this work.

Funding

This research was funded by Beijing Medical Award Foundation (YXJL-2022−0665−0210), Guangxi Key Research and Development Program (Grant No. GuikeAB2323026087) and Natural Science Foundation of Guangxi Zhuang Autonomous Region (No. 2023GXNSFAA026225).

Notes

The authors declare no competing financial interest.

■ ACKNOWLEDGMENTS

We are indebted to personnel at Guangxi Medical University for their kind technical assistance.

■ ABBREVIATIONS

SPIO, superparamagnetic iron oxide nanoparticles; PEG, polyethylene glycol; MRI, magnetic resonance imaging; ROS, reactive oxygen species; GPX4, glutathione peroxidase 4; T_2WI, T_2-weighted imaging; NPC, nasopharyngeal cancer; Cys, cystine; Glu, glutamate; GSS, glutathione synthetase; Gly, glycine; GSH, glutathione; LPO, lipid peroxidation; TFR, transferrin receptor; LIP, labile iron pool; TEM, transmission electron microscope; HPLC, high-performance liquid chromatography; DLS, dynamic light scattering; PBS, phosphate-buffered saline; RPMI-1640, Roswell Park Memorial Institute-1640; FBS, fetal bovine serum; DMEM, Dulbecco's modified Eagle's medium; PW, pure water; R6G, rhodamine 6G; DFO, deferoxamine; DCFH-DA, 2, 7-dichlorodi-hydrofluorescein diacetate; NAC, *N*-acetyl-L-cysteine; RT-qPCR, real-time quantitative polymerase chain reaction; NADPH, nicotinamide adenine dinucleotide phosphate; MDA, malondialdehyde; CCK-8, Cell Counting Kit-8; ICP-OES, inductively coupled plasma-optical emission spectrometers; H&E, hematoxylin and eosin; DHE, dihydroethidium

■ REFERENCES

(1) Wong, K. C. W.; Hui, E. P.; Lo, K. W.; et al. Nasopharyngeal carcinoma: An evolving paradigm. *Nat. Rev. Clin Oncol* **2021**, *18* (11), 679−695.
(2) Chang, E. T.; Ye, W.; Zeng, Y. X.; et al. The evolving epidemiology of nasopharyngeal carcinoma. *Cancer Epidemiol Biomarkers Prev* **2021**, *30* (6), 1035−1047.
(3) Tang, L. L.; Guo, R.; Zhang, N.; et al. Effect of radiotherapy alone vs radiotherapy with concurrent chemoradiotherapy on survival without disease relapse in patients with low-risk nasopharyngeal carcinoma: A randomized clinical trial. *JAMA* **2022**, *328* (8), 728−736.
(4) Zhang, Y.; Chen, L.; Hu, G. Q.; Zhang, N.; Zhu, X. D.; Yang, K. Y.; Jin, F.; Shi, M.; Chen, Y. P.; Hu, W. H.; Cheng, Z. B.; Wang, S. Y.; Tian, Y.; Wang, X. C.; Sun, Y.; Li, J. G.; Li, W. F.; Li, Y. H.; Mao, Y. P.; Zhou, G. Q.; Sun, R.; Liu, X.; Guo, R.; Long, G. X.; Liang, S. Q.; Li, L.; Huang, J.; Long, J. H.; Zang, J.; Liu, Q. D.; Zou, L.; Su, Q. F.; Zheng, B. M.; Xiao, Y.; Guo, Y.; Han, F.; Mo, H. Y.; Lv, J. W.; Du, X. J.; Xu, C.; Liu, N.; Li, Y. Q.; Xie, F. Y.; Sun, Y.; Ma, J.; Tang, L. L.; et al. Final overall survival analysis of gemcitabine and cisplatin induction chemotherapy in nasopharyngeal carcinoma: A multicenter, randomized Phase III trial. *J. Clin Oncol* **2022**, *40* (22), 2420−2425.
(5) You, R.; Liu, Y. P.; Xie, Y. L.; et al. Hyperfractionation compared with standard fractionation in intensity-modulated radiotherapy for patients with locally advanced recurrent nasopharyngeal carcinoma: A multicentre, randomised, open-label, phase 3 trial. *Lancet* **2023**, *401* (10380), 917−927.
(6) Tang, L. L.; Chen, Y. P.; Chen, C. B.; et al. The Chinese Society of Clinical Oncology (CSCO) clinical guidelines for the diagnosis and treatment of nasopharyngeal carcinoma. *Cancer Commun. (Lond)* **2021**, *41* (11), 1195−1227.
(7) Yan, H.; Talty, R.; Johnson, C. H. Targeting ferroptosis to treat colorectal cancer. *Trends Cell Biol.* **2023**, *33* (3), 185−188.
(8) Kang, N.; Son, S.; Min, S.; et al. Stimuli-responsive ferroptosis for cancer therapy. *Chem. Soc. Rev.* **2023**, *52* (12), 3955−3972.
(9) Zheng, S.; Guan, X. Y. Ferroptosis: Promising approach for cancer and cancer immunotherapy. *Cancer Lett.* **2023**, *561*, No. 216152.
(10) Conche, C.; Finkelmeier, F.; Pešić, M.; et al. Combining ferroptosis induction with MDSC blockade renders primary tumours and metastases in liver sensitive to immune checkpoint blockade. *Gut* **2023**, *72* (9), 1774−1782.
(11) Qi, R.; Bai, Y.; Li, K.; et al. Cancer-associated fibroblasts suppress ferroptosis and induce gemcitabine resistance in pancreatic cancer cells by secreting exosome-derived ACSL4-targeting miRNAs. *Drug Resist Updat* **2023**, *68*, No. 100960.
(12) Wang, M. E.; Chen, J.; Lu, Y.; Bawcom, A. R.; Wu, J.; Ou, J.; Asara, J. M.; Armstrong, A. J.; Wang, Q.; Li, L.; Wang, Y.; Huang, J.; Chen, M.; et al. RB1-deficient prostate tumor growth and metastasis are vulnerable to ferroptosis induction via the E2F/ACSL4 axis. *J. Clin Invest.* **2023**, *133* (10), No. e166647.
(13) Yang, F.; Xiao, Y.; Ding, J. H.; Jin, X.; Ma, D.; Li, D. Q.; Shi, J. X.; Huang, W.; Wang, Y. P.; Jiang, Y. Z.; Shao, Z. M.; et al. Ferroptosis heterogeneity in triple-negative breast cancer reveals an innovative immunotherapy combination strategy. *Cell Metabol.* **2023**, *35* (1), 84−100.e8.
(14) Wang, C. K.; Chen, T. J.; Tan, G. Y. T.; et al. MEX3A mediates p53 degradation to suppress ferroptosis and facilitate ovarian cancer tumorigenesis. *Cancer Res.* **2023**, *83* (2), 251−263.
(15) Dolma, S.; Lessnick, S. L.; Hahn, W. C.; Stockwell, B. R.; et al. Identification of genotype-selective antitumor agents using synthetic lethal chemical screening in engineered human tumor cells. *Cell* **2003**, *3* (3), 285−296.
(16) Liang, Z.; Wu, Q.; Wang, H.; Tan, J.; Wang, H.; Gou, Y.; Cao, Y.; Li, Z.; Zhang, Z.; et al. Silencing of lncRNA MALAT1 facilitates erastin-induced ferroptosis in endometriosis through miR-145−5p/MUC1 signaling. *Cell Death Discovery* **2022**, *8* (1), 190.
(17) Chen, M.; Li, X.; Du, B.; et al. Upstream stimulatory factor 2 inhibits erastin-induced ferroptosis in pancreatic cancer through transcriptional regulation of pyruvate kinase M2. *Biochem. Pharmacol.* **2022**, *205*, No. 115255.
(18) Wang, H.; Cheng, Y.; Mao, C.; et al. Emerging mechanisms and targeted therapy of ferroptosis in cancer. *Mol. Ther* **2021**, *29* (7), 2185−2208.
(19) Gan, B. How erastin assassinates cells by ferroptosis revealed. *Protein Cell* **2022**, *14* (2), 84−86.
(20) Chen, P.; Wang, D.; Xiao, T.; et al. ACSL4 promotes ferroptosis and M1 macrophage polarization to regulate the tumorigenesis of nasopharyngeal carcinoma. *Int. Immunopharmacol* **2023**, *122*, No. 110629.
(21) Huang, W. M.; Li, Z. X.; Wu, Y. H.; et al. m6A demethylase FTO renders radioresistance of nasopharyngeal carcinoma via promoting OTUB1-mediated anti-ferroptosis. *Transl Oncol* **2023**, *27*, No. 101576.
(22) Liu, Y. J.; Dong, S. H.; Hu, W. H.; et al. A multifunctional biomimetic nanoplatform for image-guideded photothermal-ferrop-

totic synergistic osteosarcoma therapy. *Bioact Mater.* **2024**, *36*, 157−167.
(23) Bhatia, S. N.; Chen, X.; Dobrovolskaia, M. A.; et al. Cancer nanomedicine. *Nat. Rev. Cancer* **2022**, *22* (10), 550−556.
(24) Lv, R.; Raab, M.; Wang, Y.; et al. Nanochemistry advancing photon conversion in rare-earth nanostructures for theranostics. *Coord. Chem. Rev.* **2022**, *460*, No. 214486.
(25) Ruan, Y.; Xiong, Y.; Fang, W.; Yu, Q.; Mai, Y.; Cao, Z.; Wang, K.; Lei, M.; Xu, J.; Liu, Y.; Zhang, X.; Liao, W.; Liu, J.; et al. Highly sensitive curcumin-conjugated nanotheranostic platform for detecting amyloid-beta plaques by magnetic resonance imaging and reversing cognitive deficits of Alzheimer's disease via NLRP3-inhibition. *J. Nanobiotechnol.* **2022**, *20* (1), 322.
(26) Lv, R.; Jiang, X.; Yang, F.; et al. Degradable magnetic-response photoacoustic/up-conversion luminescence imaging-guided photodynamic/photothermal antitumor therapy. *Biomater Sci.* **2019**, *7* (11), 4558−4567.
(27) Yuan, H.; Xia, P.; Sun, X.; Ma, J.; Xu, X.; Fu, C.; Zhou, H.; Guan, Y.; Li, Z.; Zhao, S.; Wang, H.; Dai, L.; Xu, C.; Dong, S.; Geng, Q.; Li, Z.; Wang, J.; et al. Photothermal nanozymatic nanoparticles induce ferroptosis and apoptosis through tumor microenvironment manipulation for cancer therapy. *Small* **2022**, *18* (41), No. e2202161.
(28) Liu, L.; Liu, L.; Li, Y.; et al. Ultrasmall superparamagnetic nanoparticles targeting E-selectin: Synthesis and effects in mice in vitro and in vivo. *Int. J. Nanomedicine* **2019**, *14*, 4517−4528.
(29) Liu, Q.; Liu, L.; Mo, C.; Zhou, X.; Chen, D.; He, Y.; He, H.; Kang, W.; Zhao, Y.; Jin, G.; et al. Polyethylene glycol-coated ultrasmall superparamagnetic iron oxide nanoparticles-coupled sialyl Lewis X nanotheranostic platform for nasopharyngeal carcinoma imaging and photothermal therapy. *J. Nanobiotechnol.* **2021**, *19* (1), 171.
(30) Sobhanan, J.; Rival, J. V.; Anas, A.; et al. Luminescent quantum dots: Synthesis, optical properties, bioimaging and toxicity. *Adv. Drug Deliv Rev.* **2023**, *197*, No. 114830.
(31) Guo, S.; Shi, Y.; Liang, Y.; et al. Relationship and improvement strategies between drug nanocarrier characteristics and hemocompatibility: What can we learn from the literature. *Asian J. Pharm. Sci.* **2021**, *16* (5), 551−576.
(32) Yang, S.; Wong, K. H.; Hua, P.; et al. ROS-responsive fluorinated polyethyleneimine vector to co-deliver shMTHFD2 and shGPX4 plasmids induces ferroptosis and apoptosis for cancer therapy. *Acta Biomater* **2022**, *140*, 492−505.
(33) Zhu, X.; Chen, Q.; Xie, L.; et al. Iron ion and sulfasalazine-loaded polydopamine nanoparticles for Fenton reaction and glutathione peroxidase 4 inactivation for enhanced cancer ferrotherapy. *Acta Biomater* **2022**, *145*, 210−221.
(34) Zheng, Z.; Lei, C.; Liu, H.; Jiang, M.; Zhou, Z.; Zhao, Y.; Yu, C.; Wei, H.; et al. A ROS-responsive liposomal composite hydrogel integrating improved mitochondrial function and pro-angiogenesis for efficient treatment of myocardial infarction. *Adv. Healthcare Mater.* **2022**, *11* (19), No. e2200990.
(35) Gao, D.; Huang, Y.; Sun, X.; et al. Overexpression of c-Jun inhibits erastin-induced ferroptosis in Schwann cells and promotes repair of facial nerve function. *J. Cell Mol. Med.* **2022**, *26* (8), 2191−2204.
(36) Onukwufor, J. O.; Dirksen, R. T.; Wojtovich, A. P. Iron dysregulation in Mitochondrial dysfunction and Alzheimer's disease. *Antioxidants (Basel)* **2022**, *11* (4), 692.
(37) Zhu, L.; You, Y.; Zhu, M.; Song, Y.; Zhang, J.; Hu, J.; Xu, X.; Xu, X.; Du, Y.; Ji, J.; et al. Ferritin-hijacking nanoparticles spatiotemporally directing endogenous ferroptosis for synergistic anticancer therapy. *Adv. Mater.* **2022**, *34* (51), No. e2207174.
(38) Nakamura, H.; Takada, K. Reactive oxygen species in cancer: Current findings and future directions. *Cancer Sci.* **2021**, *112* (10), 3945−3952.
(39) Wen, Y.; Chen, H.; Zhang, L.; et al. Glycyrrhetinic acid induces oxidative/nitrative stress and drives ferroptosis through activating NADPH oxidases and iNOS, and depriving glutathione in triple-negative breast cancer cells. *Free Radic Biol. Med.* **2021**, *173*, 41−51.
(40) Zhang, Y.; Tan, H.; Daniels, J. D.; Zandkarimi, F.; Liu, H.; Brown, L. M.; Uchida, K.; O'Connor, O. A.; Stockwell, B. R.; et al. Imidazole ketone erastin induces ferroptosis and slows tumor growth in a mouse lymphoma model. *Cell Chem. Biol.* **2019**, *26* (5), 623−633.e9.

https://doi.org/10.1021/acs.molpharmaceut.3c01172
Mol. Pharmaceutics 2024, 21, 2767−2780